Solid Freeform Fabrication 2022: Proceedings of the 33rd Annual International Solid Freeform Fabrication Symposium – An Additive Manufacturing Conference
Reviewed Paper

Influence of Powder Properties and Process Parameters on the High Temperature PBF-LB/M Manufacturability of Filigree Tungsten Components

Maximilian Binder[1,2*], Olgu Yücel[1,2], Thomas Bareth[1], Georg Schlick[1], Alexander von Müller[3], Jeong-Ha You[3], Birger Buschmann[1], Riccardo de Luca[3,4], Pierlugi Fanelli[4], Christian Seidel[1,5]

[1]Fraunhofer Institute for Casting, Composite and Processing Technology IGCV, Am Technologiezentrum 10, 86159 Augsburg, Germany
[2]Technical University of Munich, Institute for Machine Tools and Industrial Management, Boltzmannstr. 15, 85748 Garching, Germany
[3]Max Planck Institute for Plasma Physics, Boltzmannstr. 2, 85748 Garching, Germany
[4]University of Tuscia, DEIM Department, Campus Riello, Blocco F, 01100 Viterbo, Italy
[5]Munich University of Applied Science, Department of Applied Science and Mechatronics, Lothstr. 34, 80335 Munich, Germany
*Corresponding author: maximilian.binder@igcv.fraunhofer.de

Abstract

The production of complex lattice structures made of pure tungsten can be of great interest for potential applications in various industrial sectors such as energy technology or medical devices. One example is the plasma-facing armour of so-called limiter components in nuclear fusion power reactors, where the tungsten lattice armour is supposed to withstand extreme heat flux loads up-on transient plasma events.. The reliability of the tungsten armour is hence an important requirement for the sustainable operation of fusion power reactors [1,2].
Tungsten is difficult to process to a satisfactory degree due to its high melting point, its hardness as well as its susceptibility to cracking. Therefore, this paper presents the manner in which tungsten can be processed into fine lattice structures by means of high-temperature laser-based powder bed fusion. It also explains to what extent the used metal powder and the laser-exposure strategy have an influence on pores and component defects. It is shown how particle size distribution and sphericity of the powders have a major impact on the basic processability of the material. Furthermore, it presents to what extent the laser exposure parameters, such as the laser hatch distance, can have an influence on the resulting density of the material and which methods are used to determine the actual material density of lattice cubes in the first place. Finally, measurements of the electrical conductivity of the fabricated AM structures are presented, as this is of interest with respect to many other areas of application.

Keywords: Additive Manufacturing, High-Temperature Laser-based Powder Bed Fusion, Tungsten, Refractory Metal

Introduction

Due to its high melting point, high thermal conductivity, high threshold energy for sputtering and low tritium solubility, tungsten has been the most favored candidate for the plasma-facing material (PFM) of future magnetic confinement fusion reactors [3]. The EU demonstration fusion reactor (DEMO), which is currently in a conceptual design phase, will be equipped with a tungsten wall [1,2,4]. Some of the tungsten-based plasma-facing

components require partly complex geometries to maximize their functionality. For instance, the tungsten armour of the plasma limiter components shall be designed in form of a fine lattice structure, which can hardly be achieved through conventional machining. This is one example why additive manufacturing of such parts is in high demand in this field of technology [3,5]. Additive manufacturing (AM) processes, such as Laser-based Powder Bed Fusion (PBF-LB), provide a unique freedom of design for developers. The AM process is an automated and tool-free process for producing three-dimensional physical components directly from a 3D CAD dataset [6,7]. However, AM also reaches its limits when it comes to processing special materials such as tungsten. For example, the brittleness and high ductile-to-brittle transition temperature (DBTT) of tungsten have a major impact on pores and cracks in the final parts [8]. Nevertheless, the formation of such defects can be reduced by using a high-temperature process. Still, a satisfactory part quality is difficult to achieve today, which points out the necessity of additional research [9]. Also, great effort has been put into optimizing numerous other aspects that can significantly influence the part quality, for example properties of the raw material or machine parameters used.

Materials and Methods

The following section presents the various methods and devices used for powder and part quality analysis, including the used PBF-LB/M facility and the design of experiments.

Tungsten powder analysis

Flowability

The quality of a powder can be characterized by its flowability, which is influenced by many variables such as the particle morphology or particle size distribution. Although it is not possible to describe the flowability as a function of these variables in general, there are special measuring instruments to determine values which can describe the flowability of powders [10]. To characterize the flowability, the following quantities were determined by using the FT4 powder rheometer by Freeman Technologies: Basic Flow Energy, Stability Index, Flow Rate Index, Specific Energy and Conditioned Bulk Density.

The **Basic Flow Energy (BFE)** can be determined by measuring the work when moving a helix shaped blade downwards through a known volume of powder contained in a vessel. Depending on the type and condition of the powder, the blade experiences a certain resistance during the consolidation process. A low BFE, which results from low resistance, represents good flow properties of a powder. At the same time, a poor flowability is expected for high BFEs. The measurements can be made with non-variable and variable blade speeds [11]. For the following measurements, a non-variable blade speed was chosen.

The **Stability Index (SI)** is used to test whether a powder is affected by measuring. To determine the SI, a number of identical measurements using a constant blade speed are carried out in succession. In this study, seven measurements with a constant blade speed were conducted and the SI calculated as follows [12]:

$$SI = \frac{Energy\ Test\ 7}{Energy\ Test\ 1}$$

Energy Test 7 refers to the work done by the blade during the seventh downward traverse in mJ and Energy Test 1 during the first traverse, both with the same blade speed. An SI ≈ 1 indicates that the powder is not affected by the measurements. SI > 1 or SI < 1 indicates that a powder was affected during the measuring process. Possible reasons could be agglomeration or moisture uptake for SI > 1 and de-agglomeration or attrition for SI < 1 [12].
A powder that is moved around by a rake, for example, during an AM process will not behave the same way at all times. This is manifested by reduced flow rates in some areas and higher rates in other areas. The **Flow Rate Index (FRI)** provides information about how sensitive a powder is to flow rate. To determine the FRI, four additional measurements (measurements 8-11) were conducted, each by using a decreasing blade speed. In a second step, the results were compared as shown by the following equation [13]:

$$FRI = \frac{Energy\ Test\ 11}{Energy\ Test\ 8}$$

Energy Test 11 refers to the work done by the blade during the eleventh downward traverse in mJ and Energy Test 8 during the eighth. Different blade speeds are used for test eleven and eight. Table 1 shows typical values for the FRI and their corresponding meanings. 1.5 < FRI < 3 is the average Flow Rate Index for most powders, whereas FRI > 3.0 indicates a high flow rate sensitivity and FRI < 1 a low sensitivity. FRI ≈ 1 signifies that the powder is flow rate insensitive.

Table 1: FRI range

	Flow Rate Sensitivity	**Powder**
FRI > 3	high	very cohesive powders
1.5 < FRI < 3	average	most powders
FRI ≈ 1	insensitive	large particle size or surface treatments
FRI < 1	pseudoplastic or Newtonian	powders containing flow enhancers

The **Specific Energy (SE)** is described as the energy per gram that is needed for the displacement when lifting a powder using a helix shaped blade. In contrast to the BFE, the powder is lifted upwards to produce shear and is not consolidated. This method is carried out to determine the flow resistance of powders without putting them under compression stress and to analyze the shear forces between particles. Thus, the SE can be an indicator for powder cohesion [14]. The Specific Energy is defined as:

$$SE = \frac{Up\ Energy\ Cycle\ 6 + Up\ Energy\ Cycle\ 7}{2 * Split\ Mass}$$

Up Energy Cycle 6 refers to the energy measured during the upward movement of the sixth cycle and Up Energy Cycle 7 for the seventh cycle of a seven-cycle run, both in mJ. The split mass of the powder is given in g. Hence, the dimension of the SE is mJ/g. SE > 10 indicates high cohesion, values below 5 low cohesion, while 5 < SE < 10 indicates moderate cohesion [12].
The **Conditioned Bulk Density (CBD)** is defined as the ratio between the split mass and the split volume of a considered powder, which is shown by the following equation:

$$CBD = \frac{Split\ Mass}{Split\ Volume}$$

The dimension of the CBD is g/ml [12].

Particle Size Distribution (PSD)
To determine the PSD, the Mastersizer 3000 by Malvern Panalytical and its corresponding software Mastersizer 3000 were used. A dispersion or suspension consisting of a powder particle collective and a liquid, e.g., demineralized water, is irradiated with laser light in a measurement cell. Different scattered light patterns, caused by diffraction, are detected depending on the size of the particles. Smaller particles diffract the laser light with low intensity and larger particles with high intensity. By using mathematical algorithms, the recorded diffraction and scattered light patterns are converted into particle size distributions. In this study, a suspension of five grams of each powder and 600 ml of demineralized water were used for the PSD measurements. Each powder suspension was measured three times for a period of ten seconds and the device was cleaned three times with demineralized water after each measurement.

Microscopy
A TM3030 Plus scanning electron microscope (SEM) by Hitachi and the TM3030Plus software were used to visualize the powder particle shapes of the relevant powders. For the EDX analysis, Quantax 70 software was chosen.

PBF-LB/M using an AconityOne

The PBF-LB machine used for this study was the research unit AconityOne by Aconity GmbH. AconityOne is equipped with a 400 W laser (maximum power) with a beam diameter ranging between 80 - 500 µm. The PBF-LB unit reaches scan speeds up to 4 m/s and a minimal layer thickness of 10 µm. Furthermore, this machine provides a substrate heater creating substrate temperatures up to 800 °C. A residual oxygen content below 100 ppm can be reached by using argon as a protective gas, which floods the build space during processing [15].

Part quality analysis

The fabricated grid cubes were separated from the building platform by wire cutting. The Archimedean method, according to DIN 66137-3 (2019), was applied to determine the part density. By comparing the weight of a specimen in air (dry weight) with the weight measured in a liquid (wet weight), this method allows the determination of the absolute density of a given part. Isopropyl alcohol was used to determine the wet weight in order to guarantee a complete coating of the specimen and a deep penetration of the liquid in the complex and finely shaped cubes. Each specimen was weighed three times in air and three times in isopropyl alcohol. Since the density of isopropyl alcohol at the given temperature is known, the part density was then calculated using the following equation:

$$\rho = \frac{m_a * \rho_l\,(T)}{m_a - m_l}$$

where ρ is the part density in g/cm³, m_a the mass in grams of the specimen measured in air, m_l the mass of the specimen measured in liquid and $\rho_l\,(T)$ the density of the liquid at a given temperature in g/cm³. The temperature of the liquid was measured before weighing. The density of the specimens was additionally determined by using the gas pycnometer Ultrapyc 1200e from Quantachrome. For this purpose, the density of at least 3 samples was simultaneously measured. Therefore, the specimens were weighed beforehand and then placed in the sample cell, which was flooded with helium. The volume of the gas inside the cell was measured and then compared to the volume of the gas in an empty sample cell, which allows the true density of the specimens to be determined. For the metallographic cross section analysis, some specimens were cut in half in the building direction using wire cutting. Subsequently, all samples were cleaned with ethanol by using an ultrasonic cleaning machine, which allowed surface impurities and excess powder to be removed from the parts. The specimen that were cut in half were cold embedded using KEM 60 embedding material from ATM GmbH. Afterwards, the specimens were grinded and polished on a Saphir 530 machine from ATM GmbH. After two grinding processes, using water and diamond grinding plates called Galaxy Red and Galaxy Blue, the specimens were polished in three steps. Every specimen was cleaned using an ultrasonic cleaning machine between each of the steps to remove particles from the specimen surface. For polishing, increasingly finer plates and fabrics were used (Gamma, Zeta, Omega), together with Polycomplete Diamond suspensions for the steps of pre-polishing and polishing. A mixture of water and eposal was used for final polishing. Afterwards, the ground and polished specimens were carefully cleaned before the microscopic analysis. For the qualitative cross section analysis, the BX53M light microscope by Olympus and Stream Essentials software were used. The magnification was chosen so that relevant sections were clearly visible. While the light microscope is sufficient to make pores visible, the scanning electron microscope was used for more detailed investigations.

Methods

In a first step, the morphology of different tungsten powders is captured by using the scanning electron microscope. Then, the particle size distribution of the powders is determined, followed by the measurement of flow properties. After the selection of

specific powders, based on the powder analysis results, lattice structures are built by using the initial parameters from [16] shown in Table 2. This includes a variation of the Laser Power and Scan Speed and the fabrication of 27 specimen. Afterwards, these lattice cubes are analyzed and an adapted parameter set is selected according to the cubes with the highest quality regarding part density. In the second step an additional parameter optimization, which includes the variation of the hatch distance and outer distance, is carried out to investigate the influence on the part density. For each build job, a tungsten substrate and a substrate temperature of 600 °C is chosen to produce the specimen. In a final step, the electrical conductivity of the fabricated AM structures is measured by using the Sigmascope SMP350 eddy current meter from Fischer and the conductivity measuring device Loresta GX from NH Instruments.

Table 2: Parameter optimization variations.

	Parameter Base from [16]:	
	Laser Power in W:	*400*
	Scan Speed in mm/s:	*510 **
	Hatch Distance in µm:	*80*
	Outer Distance in µm:	*60*
	Layer Thickness in µm:	*40*
	Energy Density in J/mm³:	*245*
	Parameter optimization 1: *Variation of Laser Power and Scan Speed*	**Parameter optimization 2:** *Variation of Hatch Distance and Outer Distance*
Laser Power in W	340 – 400	400
Scan Speed in mm/s	500 – 700	570 **
Hatch Distance in µm	80	60 – 100
Outer Distance in µm	60	60 – 100
Layer Thickness in µm	40	40
Energy Density in J/mm³	152 – 250	175– 292

* scan speed optimized for bulk material

** value adapted due to analysis results of filigree lattice structures

Powder Quality

Eight powders from various powder manufacturers were examined as part of this study. The images of the analyzed tungsten powders show predominantly round and even particles as seen in Fig. 1. However, irregularities such as dents are partially visible, which stem from incomplete spheroidization of the particles. Also, single particles of granular shape appear in the images of the powders. These are either also the result of incomplete spheroidization or they are foreign particles, which already existed or stem from contamination during the powder handling process. The EOS, H.C. Starck, HC4000 and TPT tungsten powders consist of non-spheroidized particles of irregular shapes and different sizes.

The determined PSD curves are widely distributed (Fig. 2). The powder distributions are all monomodal and display their peaks in a range from 10 µm to 32 µm. Furthermore,

narrow and wide PSDs can be distinguished. Whereas the Tekna and EOS powder have the narrowest PSD, powders from LPW (UK82672 and UK81678) show a very broad PSD.

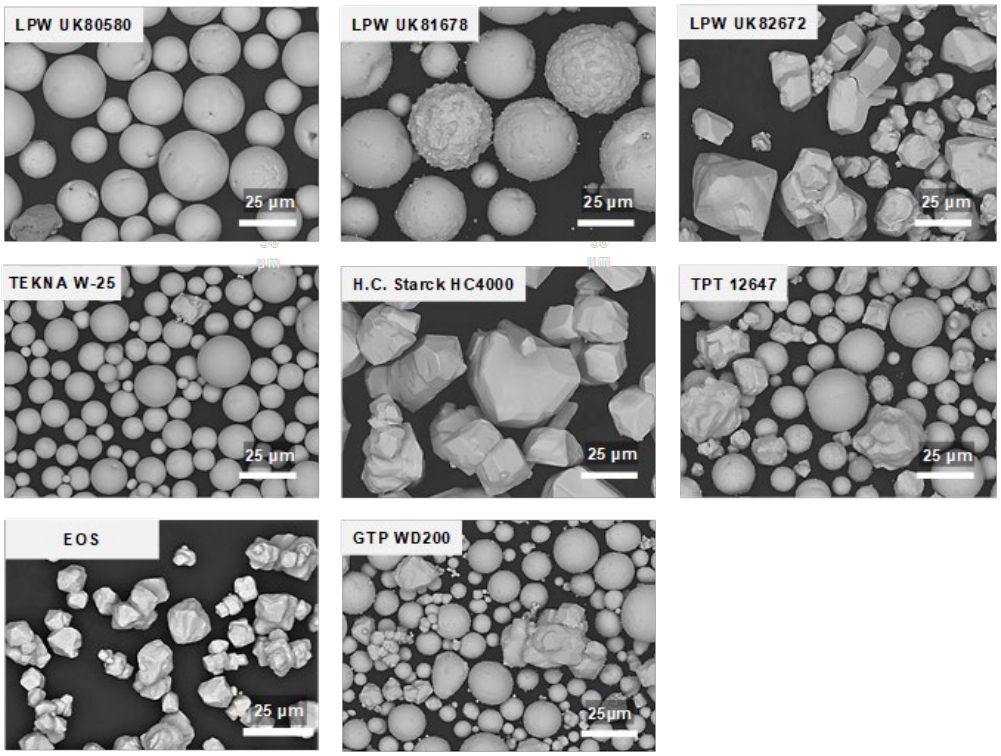

Fig. 1. SEM images of the analyzed tungsten powders.

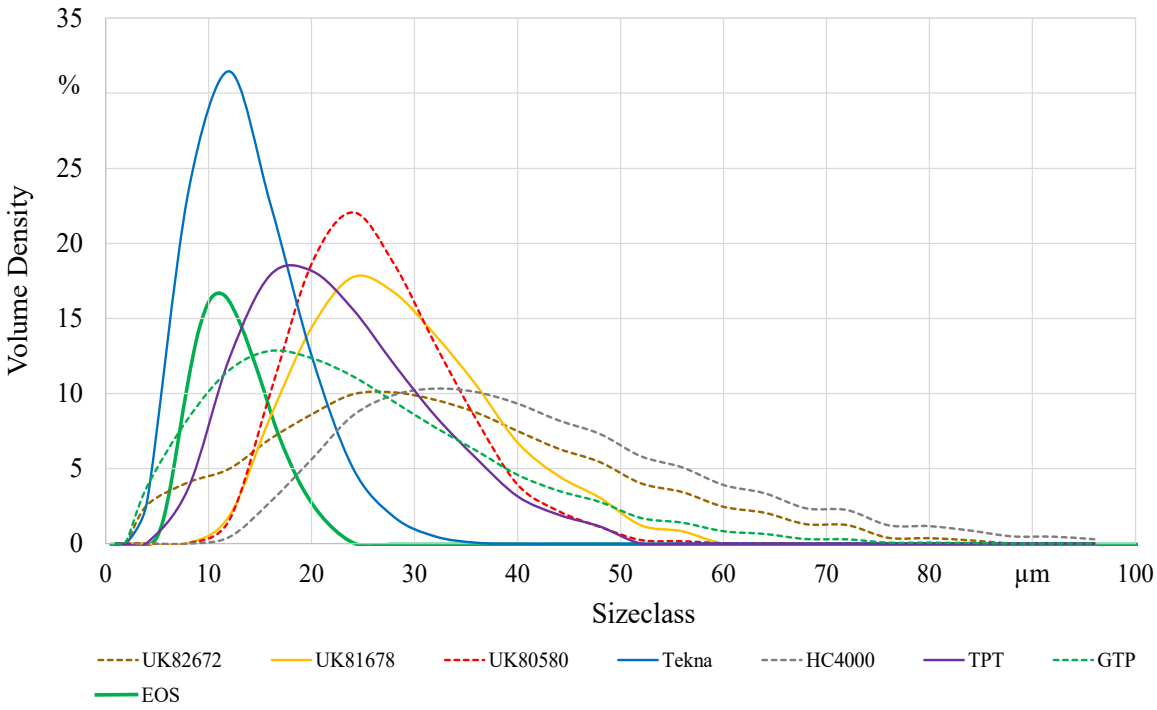

Fig. 2. PSD curves of the analyzed tungsten powders.

Table 3 summarizes the results of the flowability measurements. It shows the tendency of the Basic Flow Energy to increase for granular powders. More than two times less energy is required for the blade of the rheometer to move through the spherical Tekna powder compared to the granular EOS powder, which reaches values over 3000 mJ. The force between smaller particles is greater, which leads to higher BFEs. The BFE of the granular powders UK82672 from LPW and HC4000 from H.C. Starck show almost the same values as the EOS powder, reaching a maximum of 3477 mJ. The spherical powders range between 1250 mJ and nearly 1500 mJ. Partially spheroidized powders range around 2000 mJ. Regarding the Stability Index, most powders are settled at around SI = 1, indicating that the powders are not prone to measurement. However, the EOS powder seems to be affected by the measurements, with an SI = 1.2, assuming that possible reasons could be de-aeration, which is typical for powders with low bulk density. As air is squeezed out from the loosely packed powder, the density increases, causing more shearing between the particles, which could be the case for the HC4000 powder as well. Also, an agglomeration of particles during the measuring process can lead to an SI > 1 [12]. The Flow Rate Index for each of the measured powders reaches values between 1.05 and 1.15. According to Table 1, these powders are unresponsive to variable external forces. Continuing with the Specific Energy, the results show a tendency for higher SEs for granular powders. Spherical and partially spherical powders clearly lie under 5 mJ/g, which is an indicator for low cohesion between the powder particles. The granular powders reach values between 4.5 and 5.3 mJ/g, which is in the spectrum for moderate cohesion. This is due to higher shear forces between particles of irregular shape [14]. The results for the Conditioned Bulk Density show that the spherical Tekna powder reaches the highest density of 11.85 g/ml. The UK82672 powder has the lowest bulk density of 8.44 g/ml, which is due to the granular particle shape and the consequently loosely packed powder bed. The measurements for spherical powders result in about 25 % higher densities compared to granular powders. However, this trend should be critically viewed, as the CBD is also influenced by the PSD.

Table 3: Results of the flowability measurements of the tungsten powders.

Particle Shape	Tungsten Powder	Ø BFE in mJ	Ø SI	Ø FRI	Ø SE	Ø CBD in g/ml
Spherical	UK80580	1282.67	1.16	1.17	1.72	11.40
	UK81678	1349.33	1.00	1.06	2.02	11.33
	Tekna	1460.33	1.05	1.18	1.99	11.85
Partially spherical	TPT	1740.00	0.99	1.07	2.08	11.80
	GTP	1922.00	0.98	1.07	2.90	11.20
Granular	HC4000	3199.67	1.45	1.14	4.92	9.54
	UK82672	3477.67	1.07	1.11	5.29	8.44
	EOS	3204.01	1.20	1.15	4.55	9.17

Due to the high CBD, the Tekna powder is chosen to produce the following samples. Also, the rest of the measured values show convincing results for the Tekna powder. Furthermore, the EOS powder is chosen for comparison reasons.

Resulting Build Quality for Lattice Structures

In the first optimization step, the laser power and the scanning speed were varied using the Tekna powder. Fig. 3 shows a CAD view and built version of the investigated lattice structure.

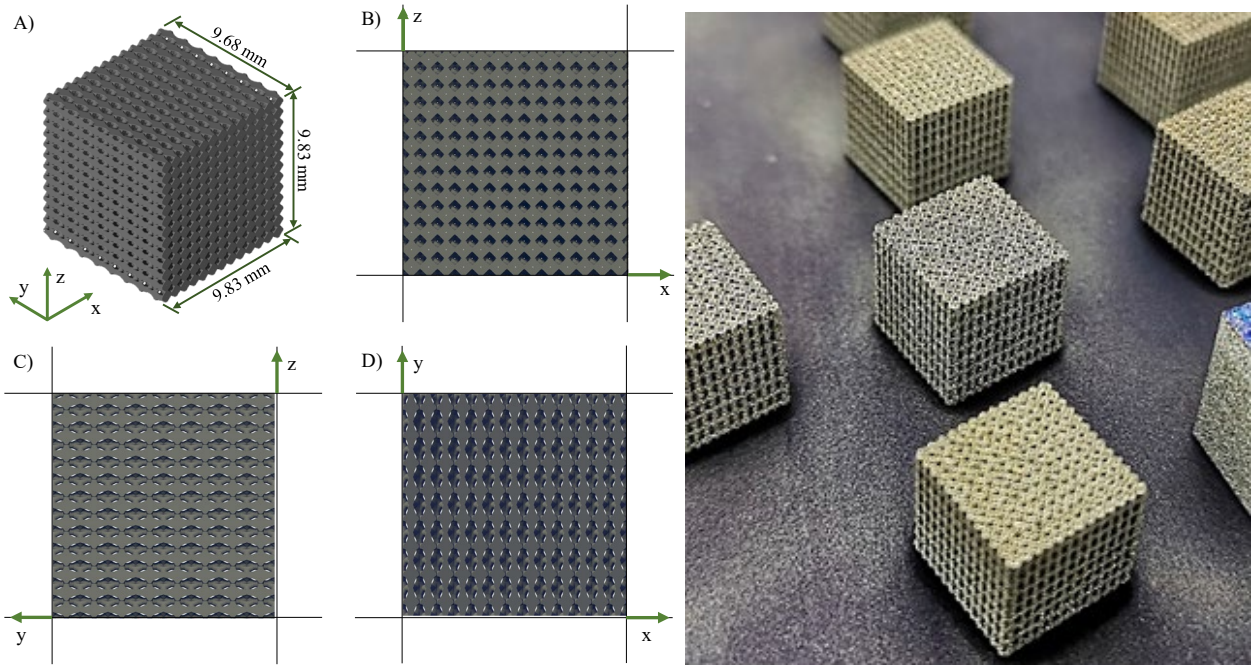

Fig. 3. Left: 3D view of lattice test specimen: A) isometric view including dimensions of the specimen, B) view of xz-plane, C) view of yz-plane, D) view of xy-plane. Right: Printed lattice-cubes on build plate.

Parameter Optimization 1

Fig. 4 shows the relative part densities of the test specimens for Parameter Optimization 1. During the investigations, it was found that density measurement of the lattice structures via Archimedes' principle becomes difficult due to the formation of air bubbles that are located in the numerous small cavities. This can distort the measurement and therefore lead to lower density values than the cubes actually have. Nevertheless, the principle provides a good basis for relative comparisons of density values.

Based on the results of Parameter Variation 1, twenty lattice-cubes are produced from two different powders using the parameters 340 W and 600 mm/s. Fig. 5 shows the results for each of the ten Tekna and ten EOS lattice-cubes. The Tekna cubes reach an average relative density of 92.02 %. Cube 1 reaches the lowest density of 90.93 %, while Cube 10 lies above 94.50 %. The results fluctuate noticeably, with a maximum difference of almost 4 %, comparing the lowest and highest values. On the other hand, the EOS cubes show significantly lower values with an average difference of over 6 % compared to the Tekna cubes. The EOS cubes have an average density of 86.38 %, with Cube 6 reaching the highest density of 86.99 % and Cube 7 the lowest value of 85.86 %.

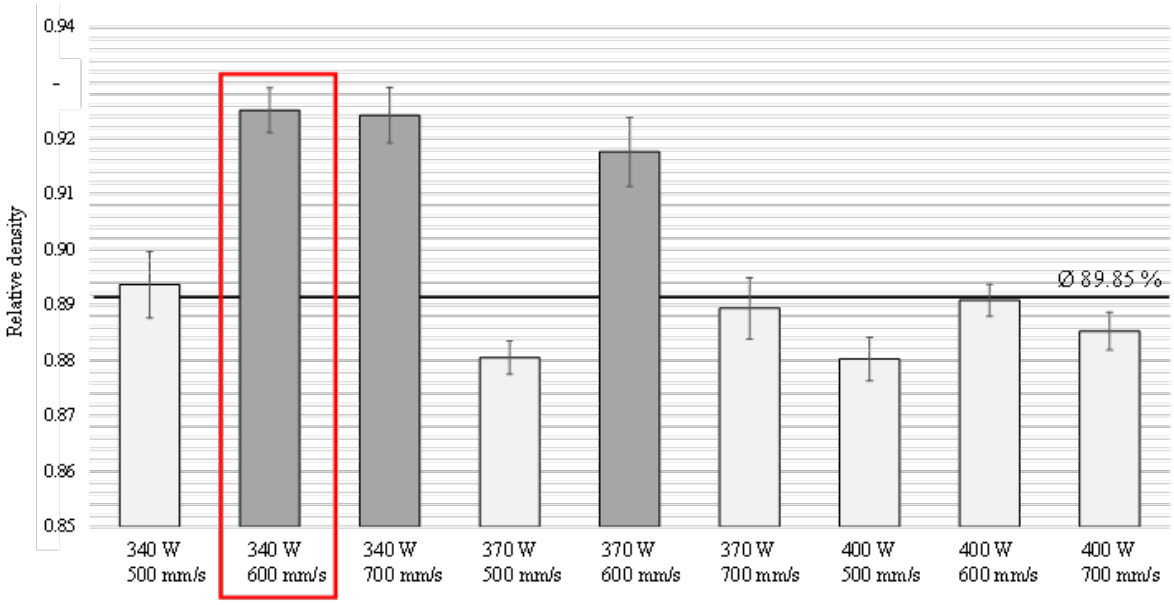

Fig. 4. Density results of parameter variation Step 1 (laser power and scan speed using Tekna-powder). Combinations of laser power and scan speed that lead to the highest densities are highlighted.

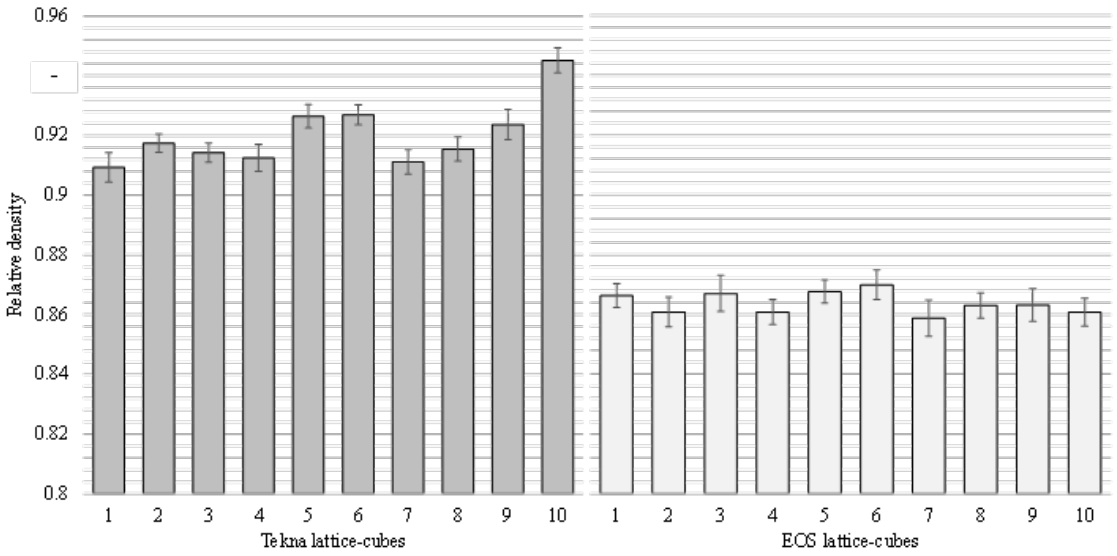

Fig. 5. Density results and comparison of lattice structures produced from Tekna and EOS powder (parameter: 340 W and 600 mm/s).

In Fig. 6 the comparison of the results of the Pycnometer and Archimedean measurements is shown. For the Pycnometer, significantly higher values for the density of the Tekna and EOS lattice-cubes with a maximum difference of almost 6 % for the Tekna Cubes 1 – 4 and almost 9 % regarding the EOS Cubes 1 – 4 are measured. The highest average density is reached by Tekna Cubes 1 – 4 with a value of 97.14 %, whereas the lowest density is measured for the EOS Cubes 5 – 7 (94.39 %). The true density of the lattice structures is expected to be between the Archimedean and Pycnometer measurement results. This is because the measurements via Pycnometer

may not be able to detect existing defects, such as cracks or open pores, as defects, but rather assume them to be the outer surface of the component and thus a higher density is measured than is actually present.

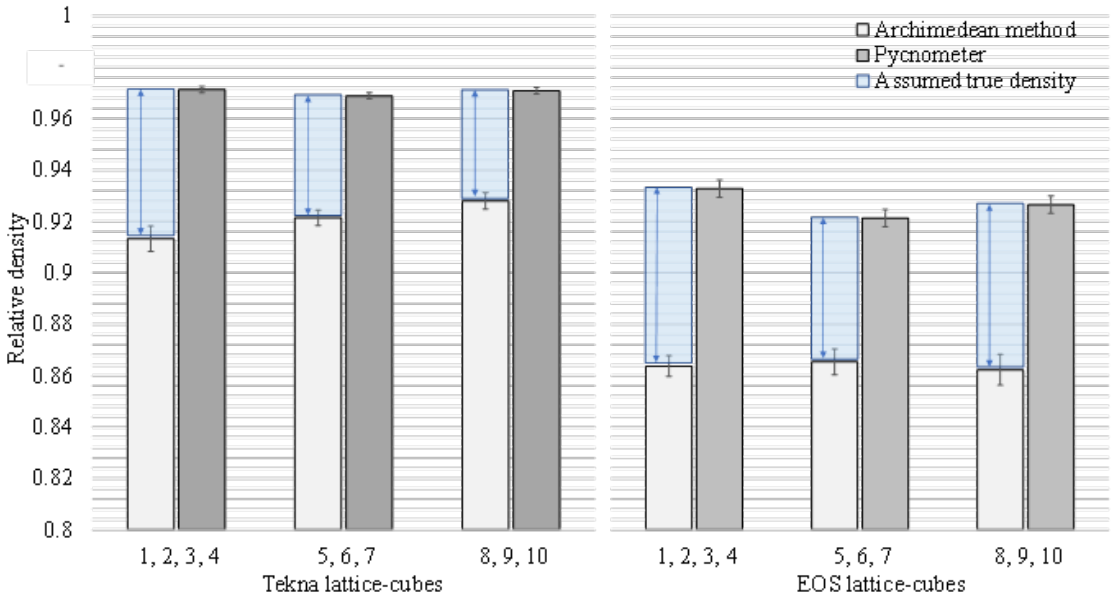

Fig. 6. Density results of lattice structures produced from Tekna and EOS powder. Comparison between density measurements using Archimedean method and Pycnometer (parameter: 340 W and 600 mm/s).

An overview of cross section images of the tungsten cubes is shown in Fig. 7. The fact that the density of grid structures is lower than that of solid components manufactured with the same parameters may be due to the fact that grid structures conduct heat less effectively via the thin structures because they have less volume. This can cause a build-up of heat, resulting in pores and cracks due to excessive temperature gradients. Here (Fig. **7**, F), it can be seen that a lack of fusion occurs between two melt tracks because the hatch distance is too large, resulting in a gap between two melt tracks. Therefore, the hatch distances have to be re-selected.

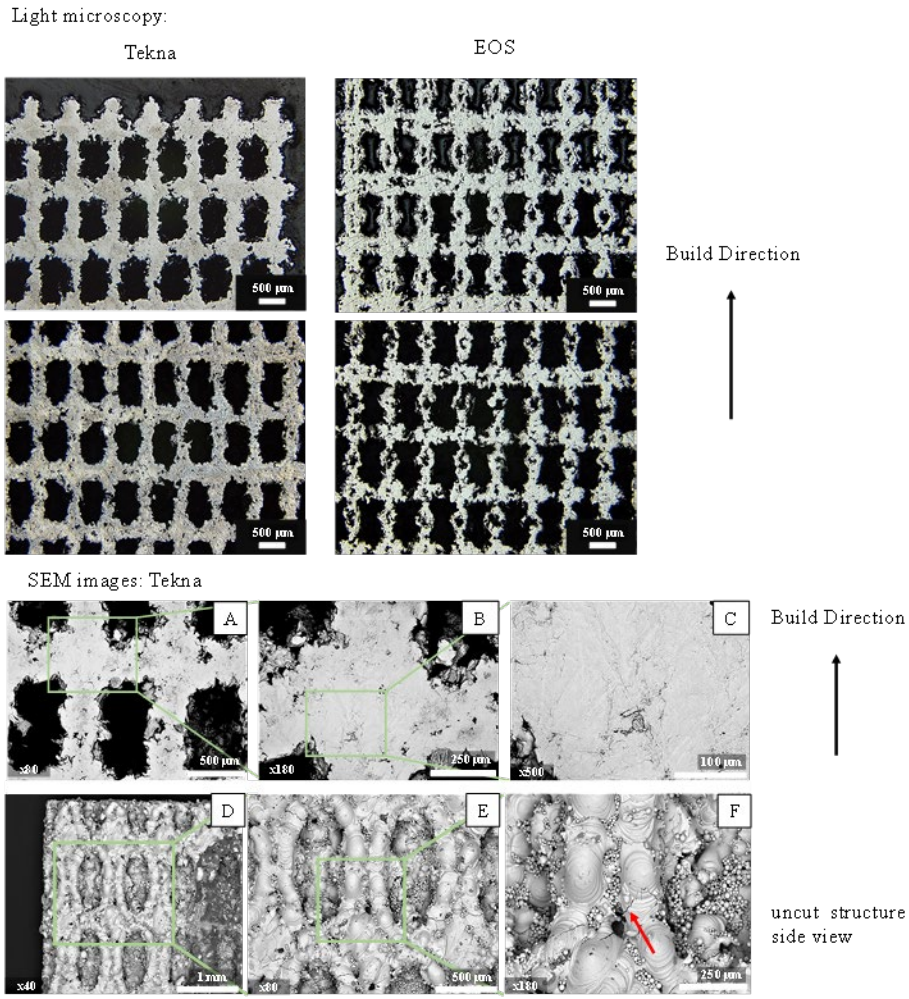

Fig. 7. Cross section images of Tekna- and EOS-powder lattice-cubes. A-C: SEM images of Tekna lattice-cubes cross sections with increasing magnification, D-F: xy-plane upskin SEM images of Tekna lattice-cubes with increasing magnification from left to right (no cross section). Nota bene: all specimen were fabricated on an Aconity One machine

Parameter optimization 2

In Parameter Variation 2, the hatch distance was investigated. The hatch distance is classified into the infill hatch distance and the outer distance as illustrated in Fig. 8 on the righthand side. The optimization was applied to minimize the porosity during the later limiter armor manufacturing. The following sample (Fig. 8 left) was built for the limiter manufacturing. Since analysis and comparability of complex lattice structures was found to be difficult during Parameter Variation 1, a representative lattice plane (xy-plane) was selected in an isolated observation.

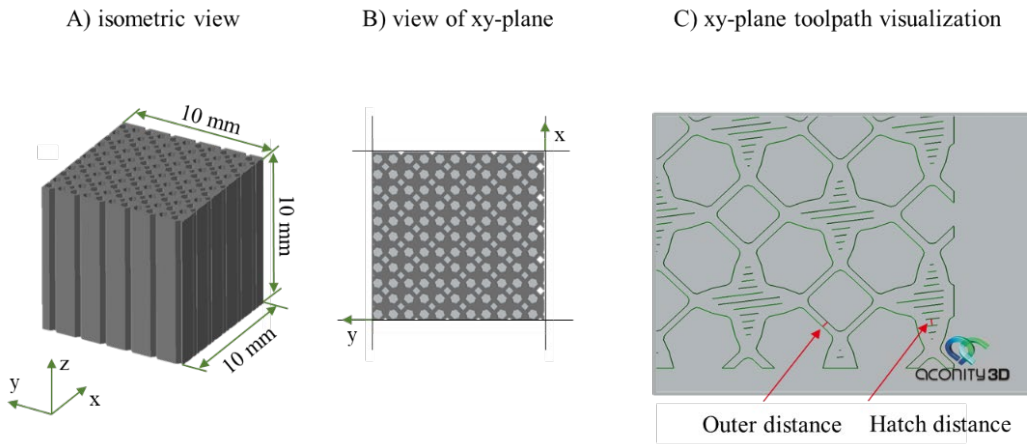

Fig. 8. View of the small-scale limiter mock-up: A) isometric view including dimensions of the specimen B) view of xy-plane C) view of xy-plane D) (Extraction of representative plane and illustration of outer distance and hatch distance with toolpath visualization).

The results of the part density (measured via Archimedes) of the test series are shown in Fig. 9. The highest part density is produced at a combination of a hatch distance at 0.10 mm and outer distance at 0.10 mm. Therefore, it can be noted that the influence of the hatch is significant and, in this case, that higher hatch distances and outer distances lead to improved densities.

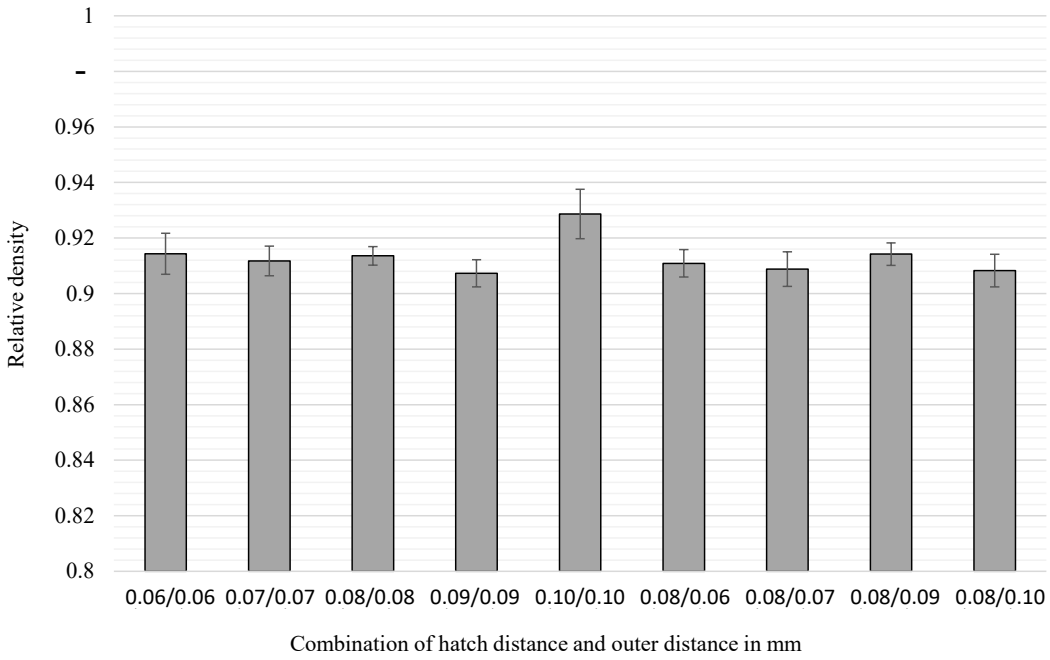

Fig. 9. Density results of Parameter Variation 2 (3 samples for each parameter variation).

The results of the electrical conductivity measurements are shown in Fig. 10. For this purpose, the electrical conductivity of conventionally manufactured solid tungsten material was compared with additively manufactured tungsten structures (Tekna powder) by using the Lorasta GX and Sigmascope SMP350 devices. The results for the conventionally manufactured tungsten samples range between 16.56 and 18.81 MS/m, which is consistent with literature values (18.2 MS/m, [17]). In comparison, the measured values

for the additively manufactured samples are significantly lower. However, this can usually be compensated for in PBF-LB/M-materials by common post-treatments for the material.

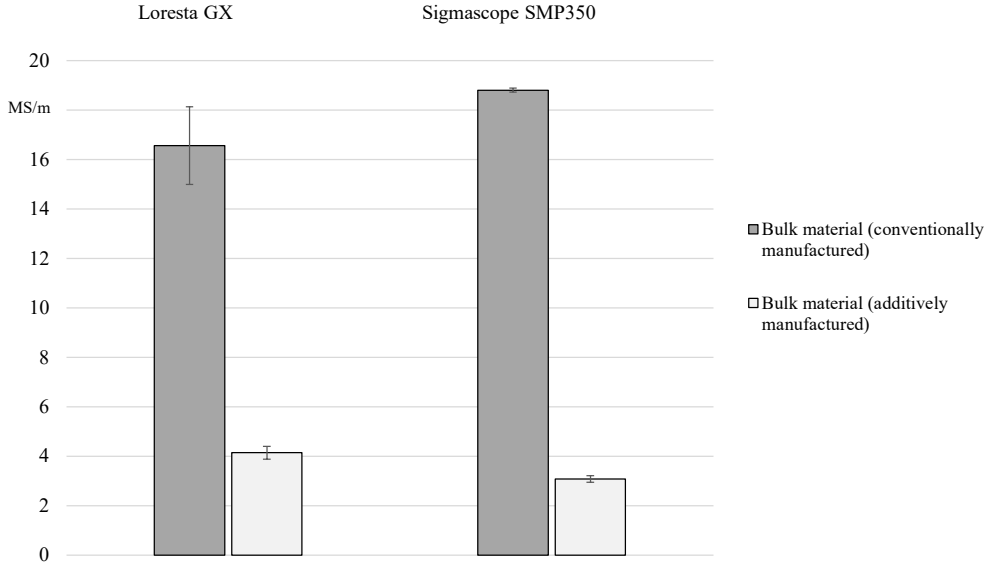

Fig. 10. Conductivity measurement results. Left: Loresta GX measurement results. Right: Sigmascope SMP350 measurement results.

Discussion

As a conclusion of this investigation, it can be noted that the optimum process parameters strongly depend on the geometry of the manufactured components (solid vs. thin walls vs. grids). Accordingly, the parameters have to be adjusted when the geometry is changed. Parameter optimization on grids exceeds standard analysis methods. They are no longer applicable to the same extent. For an improvement of the part density, it would make sense to define the laser vectors manually for a unit cell. As the investigations during the parameter optimization in the second variation showed, the arrangement of the hatches plays a significant role in the complex lattice structures. The automatic arrangement of the laser vectors by the slicing software does not lead to the desired high densities. Therefore, a further investigation would require individually fitting laser vectors (and hatch distances) for the second tested geometry. These would then have to be patterned so that whole limiter mock-ups could be produced with high densities.

Furthermore, an adaptation for the determination of the density via Archimedes was tested for the analysis of tungsten grid structures: a procedure is developed which reduces the number of gas bubbles when measuring the density of the tungsten grids. Thus, the samples are to be placed, as usual, in isopropyl alcohol for the determination of the density. Before the sample is weighed, ultrasound is applied to the container carrying the liquid and the sample. This induces the creation of air bubbles, which adhere in the grid. After an appropriate time, when no more formation of air bubbles from the sample can be noted, the measurement is carried out using Archimedes' principle (without taking the sample out of the liquid). The sample is dried for several days before it is subsequently

weighed dry. For this purpose, ten additional lattice-cubes were produced by using the Tekna powder and the optimized parameters from Variation 2. In a first step, the cubes' densities were measured as usual using the Archimedes' principle (without ultrasound treatment). Afterwards, the above mentioned adaption of the procedure was applied to determine the density. The measurement results in Fig. 11 show noticeably higher values compared to the prior results. In case of Cube No. 7, the determined density is over 2 % higher compared to the value measured before, whereas Cube No. 5 shows only a minor difference of about 0.1 %. Overall, the results show that the adaption of the determination of the density should be preferred, due to the higher values. Using the adapted method, the density results are comparable to the values measured with the pycnometer.

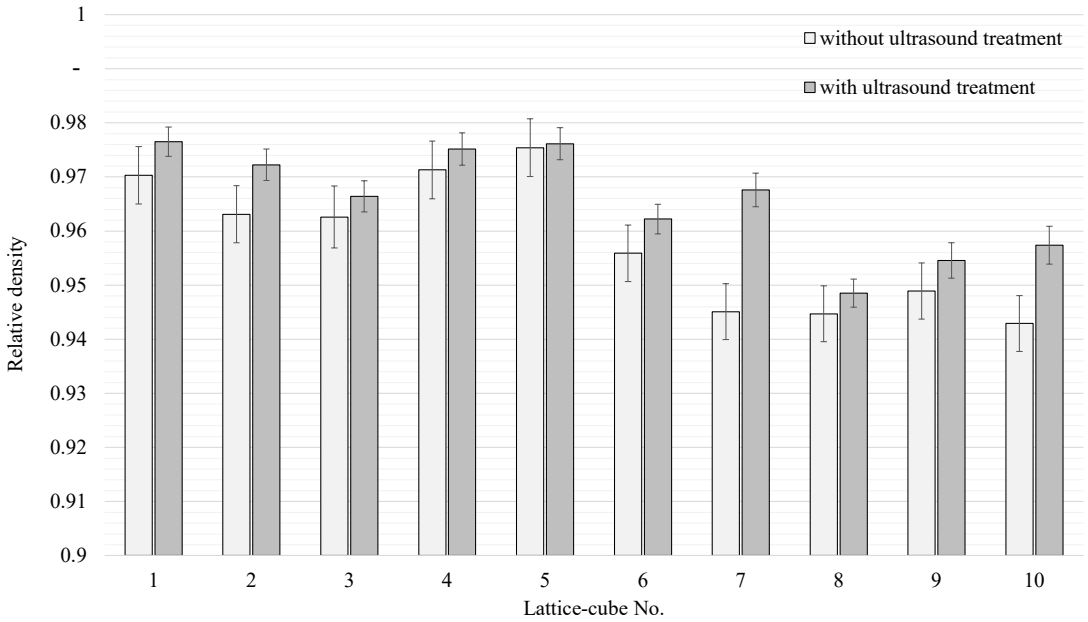

Fig. 11. Comparison of the density measurement results via Archimedean method with and without ultrasound treatment of the lattice-cubes

Summary and Outlook

In this study it was shown that lattice-cubes fabricated by using an Aconity One machine and granular powder clearly result in lower part densities compared to the cubes produced on the same machine but from spherical powder. By using the same parameters the fabrication of the granular powder resulted in more porous parts compared to spherical powders, which corresponds with the part density values. Thus, the selection of the raw material plays a crucial role regarding the part quality.

However, in the additive manufacturing of complex, thin lattice structures, the main challenge is the large number of different layers. In these layers the wall thicknesses of the struts, the degree of overhanging areas or the proportion of solid material varies considerably, which is why lattice-structures show significantly lower densities compared to bulk material. Thus, if a parameter set is to be determined that provides the best possible result for all these areas, it is often feasible for materials that can be welded well, but very challenging for tungsten structures or other refractory metals.

In the study conducted by Müller et al. [16] a parameter set was developed that is especially well suited for the fabrication of honeycomb structures and solid material areas. In this framework, the laser hatches of the honeycomb structures were designed and generated manually, which represents a significant human effort. This ensured that the laser exposure vectors met the requirements better and that a higher material density could be generated with a lower number of cracks and pores. For the fabrication of lattices, which are much more complex than the geometry of honeycomb structures, the laser hatches were automatically generated using software, as is common in additive manufacturing. This creates areas in the lattices that are exposed with less or more than the desired hatch distance. Through this study, it now stands to reason that this very factor is responsible for a higher number of pores and cracks in the structures than usual.
Thus, with a unit cell height of 1.52 mm and a layer thickness of 0.04 mm, 38 layers (number of layers = height / layer thickness) would have to be adjusted in their laser-hatch arrangement. In addition, it is a major finding that the currently available software programs are not sufficient for optimal processing of tungsten. In the further course of research, a three-stage approach would be useful in order to guarantee the highest possible quality of future manufactured samples and products:

1) Manual adjustment of laser hatches for the lattice cube geometry to verify the established thesis. The cube can then be manufactured with satisfactory quality (e.g., density > 98.5 %).
2) Derivation of hard, geometry-dependent criteria, for reliable manufacturing of tungsten grids with high densities (e.g., laser-hatch optimum for structures < 0.3 mm at h = 0.1 mm, otherwise at h = 0.08 mm).
3) Development and implementation of a suitable software solution to transfer the findings to any other type of lattice structures.

Finally, it was shown that an adaptation for the determination of the density for lattice structures via Archimedes by removing air bubbles and access powder through ultrasound is more accurate compared to the standard procedure. Therefore, a precise execution of the following steps should be carried out:

1) Placement of the samples in isopropyl alcohol
2) Applying ultrasound to the samples for an appropriate time and allowing air bubbles and access powder to be removed from the inside of the lattice-structures
3) Determination of the wet weight of the samples in the liquid
4) Drying the structures for at least 24 hours
5) Determination of the dry weight

References

[1] J.H. You, C. Bachmann, V.G. Belardi, M. Binder, D. Bowden, G. Calabrò, P. Fanelli, M. Fursdon, I.E. Garkusha, S. Gerashchenko, K. Hunger, R. de Luca, V.A. Makhlai, N. Mantel, F. Maviglia, A.v. Müller, N. Nemati, J. Roberts, F. Vivio, Z. Vizvary, K. Zhang, Limiters for DEMO wall protection: Initial design concepts &

technology options, Fusion Engineering and Design 174 (2022) 112988. https://doi.org/10.1016/j.fusengdes.2021.112988.
[2] F. Maviglia, C. Bachmann, G. Federici, T. Franke, M. Siccinio, R. Albanese, R. Ambrosino, W. Arter, R. Bonifetto, G. Calabrò, R. de Luca, L.E. Di Grazia, E. Fable, P. Fanelli, A. Fanni, M. Firdaouss, J. Gerardin, R. Lombroni, M. Mattei, M. Moscheni, W. Morris, G. Pautasso, S. Pestchanyi, G. Ramogida, M.L. Richiusa, G. Sias, F. Subba, F. Villone, J.-H. You, Z. Vizvary, Integrated design strategy for EU-DEMO first wall protection from plasma transients, Fusion Engineering and Design 177 (2022) 113067. https://doi.org/10.1016/j.fusengdes.2022.113067.
[3] J. Xie, H. Lu, J. Lu, X. Song, S. Wu, J. Lei, Additive manufacturing of tungsten using directed energy deposition for potential nuclear fusion application, Surface and Coatings Technology 409 (2021) 126884. https://doi.org/10.1016/j.surfcoat.2021.126884.
[4] J.H. You, G. Mazzone, E. Visca, H. Greuner, M. Fursdon, Y. Addab, C. Bachmann, T. Barrett, U. Bonavolontà, B. Böswirth, F.M. Castrovinci, C. Carelli, D. Coccorese, R. Coppola, F. Crescenzi, G. Di Gironimo, P.A. Di Maio, G. Di Mambro, F. Domptail, D. Dongiovanni, G. Dose, D. Flammini, L. Forest, P. Frosi, F. Gallay, B.E. Ghidersa, C. Harrington, K. Hunger, V. Imbriani, M. Li, A. Lukenskas, A. Maffucci, N. Mantel, D. Marzullo, T. Minniti, A.v. Müller, S. Noce, M.T. Porfiri, A. Quartararo, M. Richou, S. Roccella, D. Terentyev, A. Tincani, E. Vallone, S. Ventre, R. Villari, F. Villone, C. Vorpahl, K. Zhang, Divertor of the European DEMO: Engineering and technologies for power exhaust, Fusion Engineering and Design 175 (2022) 113010. https://doi.org/10.1016/j.fusengdes.2022.113010.
[5] P. Fanelli, A. Evangelisti, P. Salvini, F. Vivio, Modelling and characterization of structural behaviour of Al open-cell foams, Materials & Design 114 (2017) 167–175. https://doi.org/10.1016/j.matdes.2016.10.052.
[6] H.A. Richard, B. Schramm, T. Zipsner (Eds.), Additive Fertigung von Bauteilen und Strukturen, Springer Vieweg, Wiesbaden, 2017.
[7] A. Gebhardt, J. Kessler, L. Thurn, 3D-Drucken: Grundlagen und Anwendungen des Additive Manufacturing (AM), 2nd ed., Hanser, München, 2016.
[8] B. Vrancken, W.E. King, M.J. Matthews, In-situ characterization of tungsten microcracking in Selective Laser Melting, Procedia CIRP 74 (2018) 107–110. https://doi.org/10.1016/j.procir.2018.08.050.
[9] K. Li, G. Ma, L. Xing, Y. Wang, C. Yu, J. Chen, J. Ma, G. Wu, W. Liu, Z. Shen, X. Huang, Crack suppression via in-situ oxidation in additively manufactured W-Ta alloy, Materials Letters 263 (2020) 127212. https://doi.org/10.1016/j.matlet.2019.127212.
[10] D. Schulze, Pulver und Schüttgüter, Springer Berlin Heidelberg, Berlin, Heidelberg, 2014.
[11] Freeman Technology, The Basic Flowability Energy: W7030, 2013.
[12] Freeman Technology, Stability Method,: W7011, 2010.
[13] Freeman Technology, Variable Flow Rate Method: W7012, 2007.
[14] J. Cooke, R. Freeman, The Flowability of Powders and the Effect of Flow Additives, 2006.
[15] Aconity GmbH, Maschinen, Herzogenrath, 2022.
[16] A.v. Müller, G. Schlick, R. Neu, C. Anstätt, T. Klimkait, J. Lee, B. Pascher, M. Schmitt, C. Seidel, Additive manufacturing of pure tungsten by means of selective

laser beam melting with substrate preheating temperatures up to 1000 ◦C, Nuclear Materials and Energy 19 (2019) 184–188. https://doi.org/10.1016/j.nme.2019.02.034.
[17] H. Bernstein, Elektrotechnik/Elektronik für Maschinenbauer: Grundlagen und Anwendungen, 2nd ed., Vieweg+Teubner Verlag, Wiesbaden, 2012.